Nuclear Instruments and Methods in Physics Research B 114 (1996) 350–365

ELSEVIER

NIM B
Beam Interactions with Materials & Atoms

Beams of short lived nuclei produced by selective laser ionization in a gas cell

Yuri Kudryavtsev *, Józef Andrzejewski [1], Nathalie Bijnens, Serge Franchoo, Johnny Gentens, Mark Huyse, Andreas Piechaczek, Jurek Szerypo [2], Ils Reusen, Piet Van Duppen, Paul Van Den Bergh, Ludo Vermeeren, Jan Wauters, Andreas Wöhr

Instituut voor Kern- en Stralingsfysika, KU Leuven, Celestijnenlaan 200 D, B-3001 Leuven, Belgium

Received 19 December 1995

Abstract

An on-line laser ion source has been developed for the production of elemental and isobaric pure beams of radioactive ions. It is based on selective resonant laser ionization of nuclear reaction products thermalized and neutralized in a noble gas at high pressure. The ion source has been tested in a wide range of recoil energies going from 1.3 MeV to ~90 MeV. Efficient schemes of two step laser ionization through autoionizing states have been found for nickel, cobalt and rhodium. Residence times of the reaction products in a gas cell have been measured for helium and argon as buffer gas. Elementally pure beams of ^{54,55}Ni and ^{54}Co, produced in a light-ion induced fusion–evaporation reaction, and of ^{113}Rh, produced in proton-induced fission of ^{238}U, were obtained. An efficiency of the ion source of 6.6% for fusion reactions and of 0.22% for fission reactions has been obtained. A selectivity of the ion source of 300 for fusion and 50 for fission reactions has been achieved.

PACS: PACS number: 29.25. Ni, 32.80.F6.

1. Introduction

Modern studies of exotic nuclei far from stability at an on-line mass separator require the development of a target-ion source system that can deliver ion beams free of isobaric contamination [1,2]. The fact that these exotic nuclei have a short life time and are produced in very small quantities, usually overwhelmed by longer-lived more abundant isobars, determines the requirements of the target-ion source system: fast extraction of the reaction products, high ionization efficiency and high selectivity.

Laser resonance ionization [3,4] provides a unique possibility to develop an efficient ion source with element selectivity. In order to make it applicable to many elements, pulsed lasers are needed and consequently the radioactive atoms should be stored between the laser pulses. Storage in a hot cavity [5–7] and on a cold solid surface [8,9] has been proposed and the former approach was already used successfully at various on-line mass separators [10–12].

A few years ago, an alternative method based on resonance ionization in a gas cell was proposed [13,14] and experimentally verified [15]. It combines the fast and universal thermalization of nuclear reaction products in a buffer gas, used in He jet and ion-guide techniques [16], the high selectivity and efficiency of resonance photo-ionization and the ion-storage capacity of noble gases. The possibility of laser excitation and ionization of reaction products, thermalized in a buffer gas cell, has recently been demonstrated [17–20].

In this paper we describe the target-ion source system that was developed for the Leuven Isotope Separator On-Line (LISOL) [21] and was used for the production of isotope and element pure beams of radioactive ions produced in light ion induced fusion–evaporation and proton induced fission reactions. A high-pulse-repetition (400 Hz) laser system was used for selective and efficient ionization of radioactive Ni, Co and Rh isotopes. In the next section, we present first the basic principles of the laser ion source.

* Corresponding author. Tel: 32-16-327270; Fax: 32-16-327985; E-mail: YURI%KSF%FYS@CC3.KULEUVEN.AC.BE.

[1] Present address: Department of Nuclear Physics, University of Lodz, PL 90-236 Lodz, Poland.

[2] Present address: Institute of Experimental Physics, Warsaw University, PL-00-681 Warsaw, Poland.

PII S0168-583X(96)00194-2

This is followed by a description of the experimental set-up (Section 3). Then we describe the two-step laser ionization of stable atoms in a high pressure gas (Section 4) and present the results of on-line experiments on selective ionization of radioactive atoms produced in light-ion induced fusion–evaporation reactions (Section 5) and in proton-induced fission reaction of ^{238}U (Section 6).

2. Principles of the laser ion source

The operational principle of the ion source is based on the selective laser resonant ionization of nuclear reaction products stopped in a high-pressure noble gas [13,15]. We will describe the general principles related to the gas cell, the laser ionization and give finally the requirements to reach an optimal system. A schematic layout of the laser ion source is shown in Fig. 1. The cyclotron beam hits a thin target located in a chamber filled with noble gas. The nuclear reaction products recoiling out of the target are thermalized as neutrals or as 1^+ charged ions and move together with the noble gas in the direction of the exit hole. After a few milliseconds, most of the ions are neutralized due to recombination with plasma electrons [22] created by the primary cyclotron beam. This short ion survival time, which is the main limiting factor in the efficiency of the standard ion guide ion source, is of the order of a few ms [23]. While the atoms move towards the exit hole they pass the laser ionization zone where only the atoms of interest are ionized by the laser beams. The laser produced ions are then transported by the gas flow through the exit hole, behind which most of the gas is removed by differential pumping. The ions are directed by the negatively polarized skimmer electrode towards the extraction electrode and the analyzing magnet of the mass separator. This results in a pure beam essentially free of unwanted isotopes and isobars. The element selectivity is ensured by laser resonance ionization and the isotope selectivity by the mass separator.

Fig. 2 shows a scheme of atomic levels and possible ways for a two-step two-color ionization. The atoms thermalized in the ground state are excited by the first step laser λ_1 to an intermediate level. Then three ways are possible. The second step laser λ_2 ionizes the excited atoms through the continuum or an autoionizing state. It is also possible to excite the atoms in a high-lying Rydberg state and then these atoms are ionized via collisions with the buffer gas atoms. This ionization takes place if the electron binding energy ΔE is less than the thermal energy kT [24–26]. At room temperature, this condition corresponds to an effective principal quantum number $n^* \geq 22$. Of the three ways, the ionization through the Rydberg or autoionizing states is preferable since the photoionization cross section for these states is 10–100 times higher than for the continuum. With commercially available lasers it is possible to ionize about 80% of the elements of the periodic table using this two-color two-step scheme.

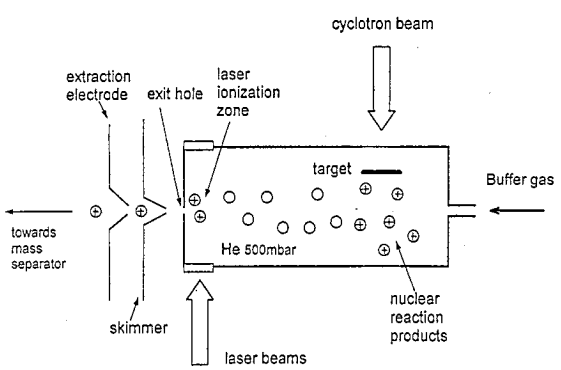

Fig. 1. Schematic layout of the laser ion source.

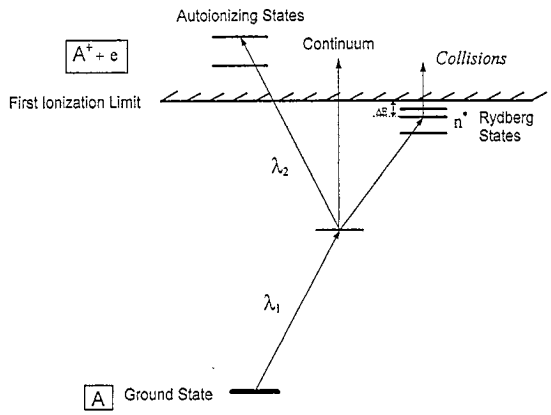

Fig. 2. An atomic level scheme showing different paths of laser resonant ionization.

In order to obtain an optimal system in the sense of maximal efficiency and maximal selectivity several requirements have to be fulfilled:

(1)The reaction products, recoiling out of the target, have to be stopped in the buffer gas.

(2)All reaction products must be neutralized in an atomic form before arriving in the laser ionization zone.

(3)Interaction with impurities can incorporate the reaction product in a molecule. If this happens during the transport to the laser interaction zone, the radioactive nuclei are lost as neutral molecules. If this happens after laser ionization, the ions can be lost in molecular side bands.

(4)Diffusion to the wall can lead to sticking of the reaction products to the wall. The evacuation time should be shorter than the mean diffusion time to the wall.

(5)The evacuation time should be shorter than the lifetime of the radioactive isotope.

(6)The pulse repetition rate of the lasers has to be chosen in such a way that the time between the subsequent pulses is smaller than the evacuation time of the ions produced in the laser ionization region.

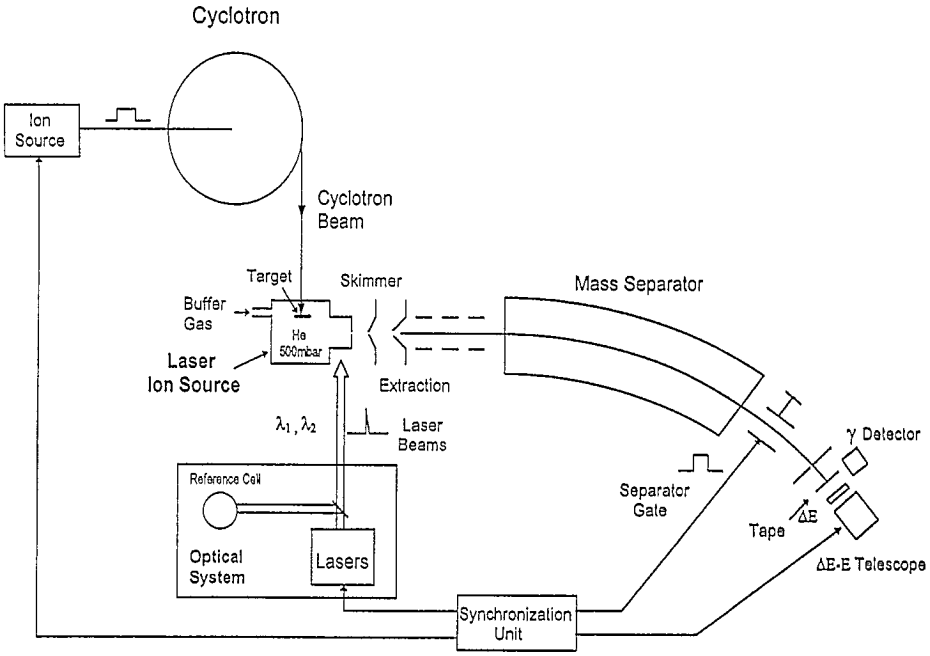

Fig. 3. Scheme of the laser ion source set-up at LISOL.

(7)The survival time of laser produced ions has to be longer than their evacuation time.

In the next paragraphs we will discuss to what extent these requirements can be fulfilled.

3. The laser ion source setup at LISOL

The laser ion source has been installed at the front end of the mass separator LISOL, which is coupled on-line to the isochronous cyclotron CYCLONE at Louvain-la-Neuve [21]. Fig. 3 shows the general layout of the laser ion source setup.

3.1. The cyclotron

The cyclotron delivered $^{3}He^{2+}$ beams with an energy of 45 MeV to test the laser ion source for a light-ion induced fusion–evaporation reaction and a $^{1}H^{+}$ beam with energy 65 MeV for a proton-induced fission reaction. The cyclotron beam could be time-modulated. Beam currents up to 1 pμA were used.

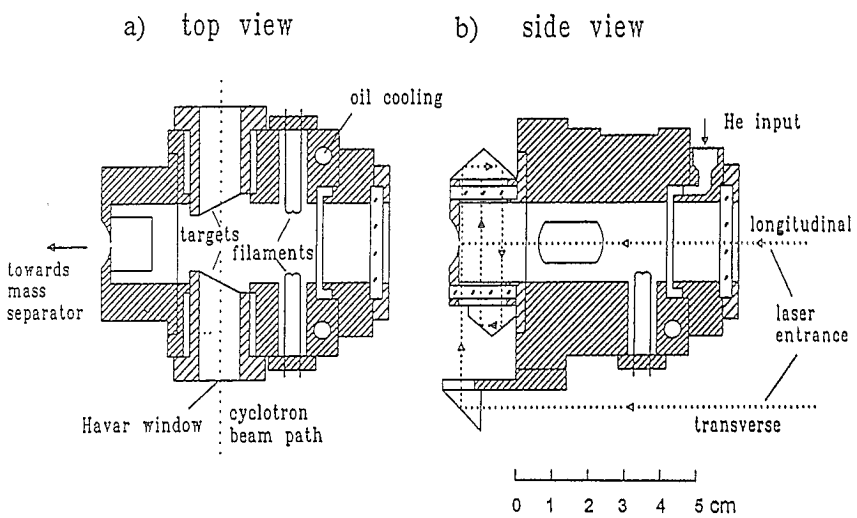

Fig. 4. Design of the on-line laser ion source. Only the set-up with the uranium targets is shown.

3.2. The laser ion source

Horizontal vertical and cuts of the laser ion source are shown in Fig. 4. The body of the cell, with an inner diameter of 2 cm, is made of brass. The cyclotron beam enters the source through a 5 μm Havar window and hits one or two targets. Reaction products recoiling out of a target are thermalized in a helium or argon buffer gas. The buffer gas enters the cell in an axially-symmetric way and moves laminarly into the direction of the exit hole, which has a diameter of 0.5 mm. With this diameter, the conductance of the exit hole is equal to 112 cm^3/s for He and 35 cm^3/s for Ar. The cyclotron beam crosses the cell on a distance of 29 mm from the exit hole.

A beam of stable nickel ions can be obtained by laser ionization of nickel atoms produced by resistive heating of a nickel filament. During the off-line tests, the filament temperature was monitored by a photodiode and the emission of nickel atoms was maintained at a steady level, however the absolute number of nickel atoms evaporating from the filament could not be determined.

3.2.1. Optical multipass system

The laser beams can enter the source in two ways, longitudinally or transversely (Fig. 4). In the first case the laser beams enter the cell through a quartz window and ionize the atoms along the axis of the cell. In most of the on-line experiments we used transverse entrance and a multipass optical system. It allows to ionize atoms in a bigger volume using the same laser energy density as the laser beams intersect the atomic flow several times. The laser beams are directed by the multipass optical system consisting of two 90° quartz prisms. This set-up can be applied for ionization of any element, independently of the laser wavelengths. The diameter of the first-step laser beam is equal to ~6 mm while the second-step laser beam has a diameter of ~4 mm.

3.2.2. The target

Two types of targets were used. In the case of proton-induced fission, two ^{238}U targets (10 mg/cm^2 each) were installed at an angle of ~30° relative to the cell axis (Fig. 4a) in order to increase the stopping efficiency of the high-recoil energy fission reaction products and to stop the reaction products further from the exit hole. In the case of light-ion induced fusion–evaporation reaction an enriched ^{54}Fe target (3 mg/cm^2) was used. It was located at a distance of 12 mm from the cell axis and perpendicular to the cyclotron beam (not shown on Fig. 4).

3.3. The laser optical system

The scheme of the laser optical system is shown in Fig. 5. Two excimer XeCl lasers with wavelength $\lambda = 308$ nm (Lambda Physik LPX240i), pump two dye lasers (Lambda Physik Scanmate 2). Both excimer lasers are synchronized to a precision of a few ns. In our experiments we used Coumarin 47 dye for the first step laser and Coumarin 153 or Coumarin 102 for the second step laser. The pulse width of the dye lasers is equal to 15 ns. The spectral band width of the dye laser radiation is equal to 0.15 cm^{-1}. In order to get light in the region of 230 nm, the radiation from the first step laser is frequency doubled in the second harmonic generator (SHG). After doubling, the band width is

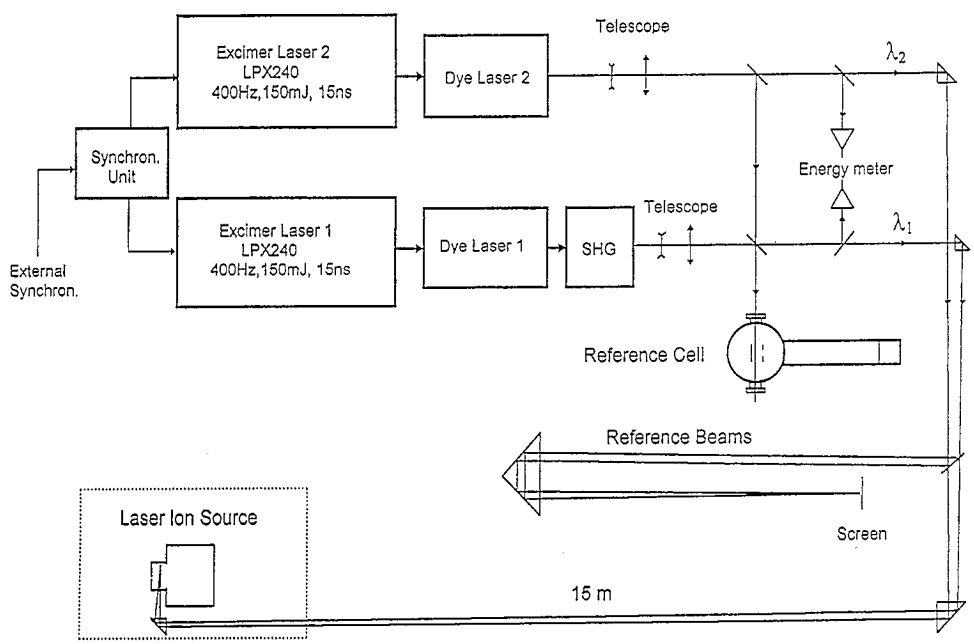

Fig. 5. Scheme of the laser optical system.

equal to 0.25 cm^{-1}. The laser beams are focused by telescopes and directed by a set of prisms into the ion source located at a distance of 15 m from the laser optical system. To control the position of the laser beams inside the ion source, reference beams (Fig. 5) are monitored on a screen located at an effective distance of 15 m.

To tune the laser wavelengths in resonance with the atomic transitions and to keep them tuned during the experiment, a fraction of the laser beams is deflected by quartz plates and directed into a reference cell. It consists of a vacuum chamber in which an atomic beam is produced by evaporating the investigated element from a resistively-heated crucible. The laser beams ionize the atoms and the obtained ions are accelerated by a pulsed voltage (10 ns, 4 kV) towards a time of flight mass spectrometer. The mass-separated ions are detected by a secondary electron multiplier.

3.4. The mass separator

The ions extracted from the ion source are accelerated to an energy of 50 keV (Fig. 3). The accelerated ions are then separated according to their mass over charge ratio in a 55° dipole magnet with a radius of 1.5 m; a mass resolving power ($R = M/\Delta M$) of 300 is obtained. The ion beam at the exit of the mass separator can be switched on and off by an external gate.

3.5. Detection of the radioactive nuclei

After mass separation, the radioactive isotopes are implanted in a movable collector tape of 6 mm width. For the detection of the beta-particles a $\Delta E - E$ telescope, consisting of a thin silicon surface barrier detector (400 μm thickness and an active surface of 150 mm^2) and a plastic scintillation detector (NE102, length 5 cm) are used. In later experiments the silicon detector was exchanged by a plastic ΔE-detector (NE104, thickness 1 mm, active surface of 706 mm^2). This yielded in a considerably higher β-detection efficiency (ca. 12% for $\Delta E - E$ coincidences). Gamma-rays are measured by a 70% high purity Ge-detector. ΔE_β and γ-rays are recorded as singles spectra. In addition ΔE_β–E_β–γ–TDC coincidences are recorded in event by event mode. The counting system can be gated by external pulses in order to synchronize it with the cyclotron and the laser beams.

3.6. The timing

The timing of the whole setup is shown in Fig. 6. A clock system pulses the cyclotron beam and produces trigger signals with variable delay relative to the cyclotron pulse for the lasers, the mass separator and the detection system. The laser beams can probe the appearance of radioactive atoms close to the exit hole of the ion source as a function of delay time relative to the cyclotron pulse. In this case, the multipass system is removed and the laser beams pass the source only once. By changing the timing of the separator gate or the laser pulse delay it is possible to investigate, for example, the influence of the cyclotron beam on the ionization of stable nickel atoms. A reduction of the background evoked by fast neutrons can be performed by antigating the detection system with the cyclotron beam. Using helium as a buffer gas, the typical value for the beam "ON" and "OFF" period of the cyclotron beam is 40 ms. The maximum efficiency of the ion source is achieved at the highest laser pulse repetition rate, 400 Hz. At these rates, the lasers are no longer synchronized with the cyclotron beam. During the radioactive life-time measurements an additional macro separator beam ON-OFF structure is imposed on the mass separator beam (for ^{55}Ni, 1 s ON, 2 s OFF).

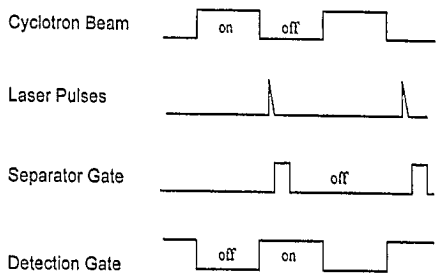

Fig. 6. Timing of the cyclotron beam, the lasers, the mass separator beam and the detection system.

4. Two-step laser ionization of stable atoms

The efficient laser resonant ionization of atoms can be performed by a two-step excitation scheme. To ionize elements that have a high ionization potential (> 7 eV) at least one of the dye laser beams should be frequency doubled. Since the first transition from the ground state to the intermediate level is usually much stronger than transitions towards Rydberg or autoionizing states, the most effective schemes are those that employ the frequency doubling in the first step. In this case, the full power of the dye laser can be used to saturate the second step transition. Unfortunately, very little is known about autoionization energy levels and transitions towards them. Extensive studies of different optical schemes for nickel, cobalt and rhodium have been performed to find the most efficient ones. Fig. 7 shows examples of scans of the second step laser wavelength λ_2 while keeping the first step laser λ_1 fixed to the resonance wavelength. Ionization through Rydberg states turned out to be less efficient than via autoionizing states. A structure just above the ionization limit was discovered. The width of the observed autoionizing lines was more than 10 cm^{-1} indicating a short life time and hence an effective ionization can be achieved. Table 1 presents wavelengths and energy levels of Ni, Co

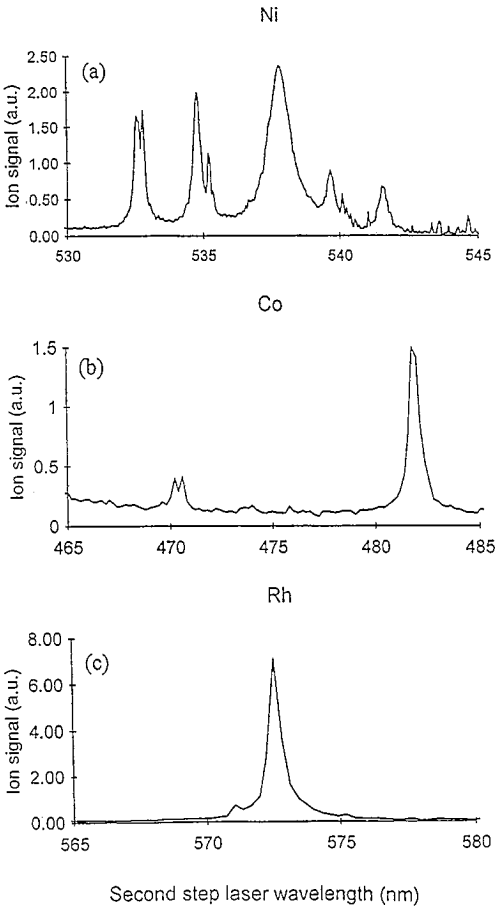

Fig. 7. Scans of the second step laser above the ionization limit for Ni, Co and Rh. The first step laser was tuned to the resonance wavelengths: Ni–232.002 nm, Co–230.903 nm, Rh–232.258 nm. The ionization limit corresponds to the following wavelengths: Ni–539.5 nm, Co–493 nm, Rh–582.5 nm.

and Rh that have been chosen for the on-line experiments. It has been found that the highest yield of Co ions can be obtained by using the following wavelengths: $\lambda_1 = 240.725$ nm, $\lambda_2 = 454.8$ nm. In spite of the slightly better results for $\lambda_1 = 240.725$ nm, we preferred the $\lambda_1 = 230.903$ nm scheme during the on-line runs because then the same dye as for nickel can be used, which allows a flexible switching between cobalt and nickel.

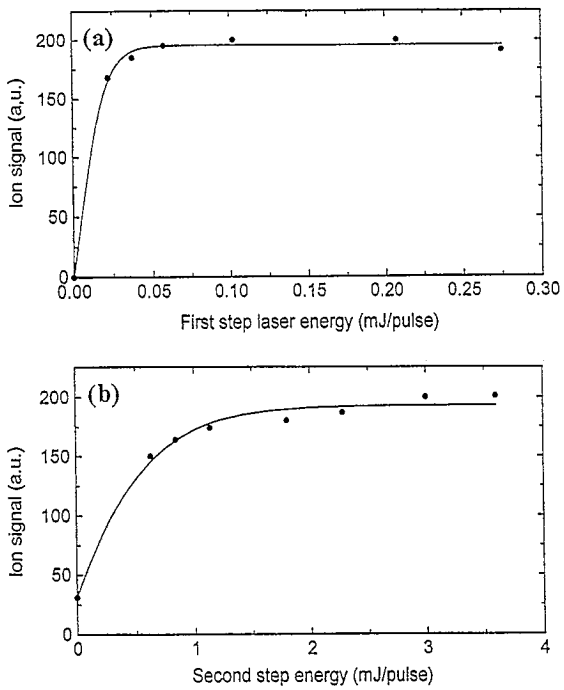

Fig. 8. Dependence of the laser produced Ni^+ signal after mass separation (mass 58) as a function of the first step (a) and the second step (b) laser pulse energy. Laser pulse repetition rate is 200 Hz.

The chosen atomic transitions can be saturated with the available laser power. Fig. 8 shows the saturation curves of the first and the second transition in Ni. These curves were measured after mass separation at mass $M = 58$, the most abundant stable Ni isotope. It is clear from Fig. 8 that the first step is completely saturated and that also for the second step not much can be gained if more laser power would be available. Actually, the slow rising of the ion signal with increasing second step laser energy (Fig. 8b) is not due to the absence of saturation but due to increasing of the volume in which the saturation of the second step takes place. This effect is not observed in the first step as the size of the first step laser beam is bigger than that of the second step. The saturation of the curves indicates that all atoms in the irradiated volume are indeed ionized.

Excitation and ionization of radioactive atoms is carried

Table 1
Transitions used for two step laser ionization of Ni, Co and Rh. λ_1, λ_2-wavelengths of the first and second step transitions, E_1, E_2 – energies of the intermediate and autoionizing levels, f_{01} – absorption oscillator strength

	First step				Second step		Ionization limit
	λ_1 (nm)	$E_0 - E_1$ (cm^{-1})		f_{01}	λ_2 (nm)	E_2 (cm^{-1})	cm^{-1} (eV)
Ni	232.003	0–43090	$^3F_4 \rightarrow {}^3G_5^0$	0.69	537.84	61678	61619 (7.64) [27]
Co	230.903	0–43295	$^4F_5 \rightarrow {}^4F_5^0$	0.045	481.90	63787	63565 (7.88) [27]
Rh	232.258	0–43042	$^4F_{9/2} \rightarrow ?$	–	572.55	60503	60200 (7.46)

Table 2
The isotope shift, the atomic line broadening and the laser bandwidth of the first step transition ($\lambda_1 = 232$ nm) in nickel

Isotope shift, $\Delta\nu_{is}$	< 0.004 cm^{-1}	for $\Delta M = 1$
Doppler width, $\Delta\nu_D$	0.07 cm^{-1}	$T = 300$ K, $M = 55$
Pressure broadening, $\Delta\nu_{Pr}$	~ 0.5 cm^{-1}	$k_{pr} \cong 0.001$ cm^{-1}/mbar, $P = 500$ mbar
Power broadening, $\Delta\nu_{Pow}$	~ 0.1 cm^{-1}	$E_1 \cong 10^5$ W/cm^2, $\tau = 15$ ns
Laser band width, $\Delta\nu_l$	~ 0.25 cm^{-1}	

out in the presence of a high-pressure buffer gas. This causes broadening of the absorption lines. The various contributions to the line broadening of the first transition for nickel are evaluated in Table 2. The spectral profile of a Doppler-broadened line at a light frequency ν_0 is a Gaussian distribution. The full width at half maximum (FWHM) is given by

$$\Delta\nu_D = 7.16 \times 10^{-7}\nu_0(T/M)^{1/2}\,[\mathrm{cm}^{-1}],$$

where ν_0 is the light frequency (in cm^{-1}), M is the atomic weight (in AMU) and T is the absolute temperature (in K). The profile of a pressure-broadened as well as a power-broadened line is given by a Lorentzian distribution. The half-width of a pressure-broadened line $\Delta\nu_{Pr}$ is proportional to the buffer gas pressure P

$$\Delta\nu_{Pr} = k_{Pr}P\,[\mathrm{cm}^{-1}],$$

where k_{Pr} is of the order of 10^{-3} cm^{-1}/mbar for resonance transitions [28]. The broadening of a spectral line due to the excitation by strong laser light (power broadening) is determined by the Rabi frequency Ω_0. For the strong Ni transition $\lambda_1 = 232.003$ nm (absorption oscillator strength $f_{01} = 0.69$), the power-broadened half-width [4] can be calculated by using the formula

$$\Delta\nu_{Pow} = \Omega_0/\pi = 10^7(I)^{1/2}\,[\mathrm{Hz}],$$

where I is the laser power density in W/cm^{-2}. The width of the second step transition is defined by the 537.84 nm autoionization line, $\Delta\lambda_2 = 0.9$ nm or $\Delta\nu_2 = 31$ cm^{-1}.

It is of interest to compare the isotope shift with the laser bandwidth and the different mechanisms of absorption broadening. For atoms in the middle of the periodic table ($50 < M < 120$) the relative isotope shift $\Delta\nu_{i.s.}/\nu_0$ is of the order of 1×10^{-7} per AMU [29]. For transitions in the wavelength region of 230 nm this corresponds to $\Delta\nu_{i.s} \sim 0.004$ cm^{-1}. Even for isotopes 20 neutrons away from the stable one the isotope shift is not bigger than 0.1 cm^{-1}. As can be seen from Table 2, the isotope shift is less than the first step laser bandwidth and less than the pressure and power broadening. This was confirmed experimentally by scanning the first step laser frequency for different stable nickel isotopes ($M = 58,60,61,64$). Consequently, during the on-line experiment it is sufficient to keep the laser frequencies in resonance with any stable isotope in the reference cell.

With the laser beams entering the ion source longitudinally, a typical stable nickel ion time signal as in Fig. 9a is obtained: a large fast component ($t < 5$ ms) from ionization close to the exit hole, followed by a much smaller slow component from ionization in the rest of the cell. The typical duration of the signal in helium is equal to 40 ms, corresponding to the evacuation time of Ni ions created on the axis of the cell next to the Ni filament. It has to be noted that the number of nickel atoms evacuated during the first 5 ms is approximately equal to the number of atoms evacuated during the next 40 ms. If the laser beams enter the cell transversally in the exit hole region, obviously only the fast component is left (Fig. 9b). In this case the cut off time is equal to 5 ms. This value corresponds to the evacuation time of ions created in the region close to the exit hole. It has to be noted that, if a high level of impurities is incorporated on purpose into the ion source, the fast component disappeares. This is explained by the reaction of nickel atoms during their transport from the filament to the exit hole. Actually even in case of a pure system, it has been found that a considerable fraction of resonantly-produced ions consisted of molecular ions, with roughly the same time profile as the Ni^+ ions (only the rising time is somewhat longer). Fig. 10 shows a mass spectrum of the laser produced ions. Typically about 30% of the ions were extracted from the source as NiH_2O^+ ($M = 76$, this corresponds to the most abundant nickel isotope $M = 58$) and a much smaller fraction as $NiHO^+$

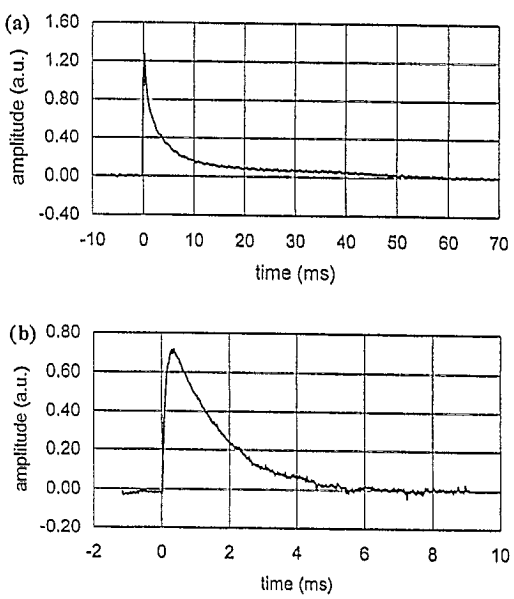

Fig. 9. A typical stable nickel time signal after mass separation ($M = 58$) with (a) longitudinal laser beams entrance and (b) transverse entrance (only one laser passing through the cell was used). The buffer gas is helium.

($M = 75$), NiN_2^+ ($M = 86$), $Ni(H_2O)_2^+$ ($M = 94$), Ni_2^+ ($M = 116$) and $Ni_2H_2O^+$ ($M = 134$). This can be explained by the following process: Ni atoms are released from the filament and diffuse all over the cell without too many losses, but after being resonantly ionized, the photoions have a much larger probability to react with impurities to form molecular ions. It is known that positive metal ions can form a sequence of molecular ions with water, e.g. $Ni(H_2O)_n^+$. The molecular ions are formed in the reaction

$$Ni^+ + H_2O + He \rightarrow NiH_2O^+ + He.$$

The exact value of the formation rate constant k_f is not known for Ni^+. By analogy to similar reactions for other ions [30], k_f could be equal to 10^{-29} cm^6/s. At a water concentration c in helium on the level of 1 ppm (10^{-6} [He]) and a helium pressure of 500 mbar, the reaction time $\tau_f = (k_f\, c\, [He]^2)^{-1}$ is equal to 0.55 ms. If the presence of NiH_2O^+ inside the cell is long enough, new water molecules can add to the formed ion. For the Ni-water molecular ions, the binding energy of subsequent ligants is roughly similar to the previous ligand [31]. They are equal to 1.78 eV for NiH_2O^+ and 1.66 eV for $Ni(H_2O)_2^+$. Note that the observed mass spectrum (Fig. 10) does not represent the real proportion between nickel and molecular ions leaving the ion source: ions are accelerated in the high pressure region between the ion source and the skimmer electrode, so molecular ions can dissociate back into their components [32]. This dissociation explains partly the poor mass resolving power ($M/\Delta M \sim 300$) of our system: the position at the focal plane of e.g. the mass 58 depends on the way the ions have passed the voltage drop when going from the high pressure region to the low pressure region. By increasing the skimmer voltage (from 100 V to 1000 V) the mass 58 peak broadens leading even to a splitting, where one part of the mass doublet represents the original Ni^+ ions and the other component stems from Ni^+ ions that originally were bound to one or several molecules. Recently we have replaced the skimmer differential pumping system by the so-called SextuPole Ion Guide (SPIG) [33,34]. In this setup the ions are guided from the high-pressure zone into the low-pressure region by a RF field applied on six rods. No acceleration takes place in the high-pressure region leading to an excellent mass resolving power ($M/\Delta M \sim 1400$, [34]). A drawback of this system is the fact that the water bonds are not destroyed and consequently that much more ions are in the molecular side bands.

5. Laser ionization of radioactive atoms produced in light-ion induced fusion–evaporation reactions

5.1. The A = 55 nickel isotope

A 45 MeV ^{3}He beam was used to produce ^{55}Ni atoms on an enriched ^{54}Fe target by the reaction ^{54}Fe(^{3}He,2n)^{55}Ni. After passage through an energy degrader and the front entrance windows, the beam on the target had an energy of 25 MeV. A cross section calculations for this reaction were performed with the HIVAP code [35] yielding a maximum cross section of 1.5 mbarn at a ^{3}He beam energy of 25 MeV. The recoil energy of the ^{55}Ni nuclei is

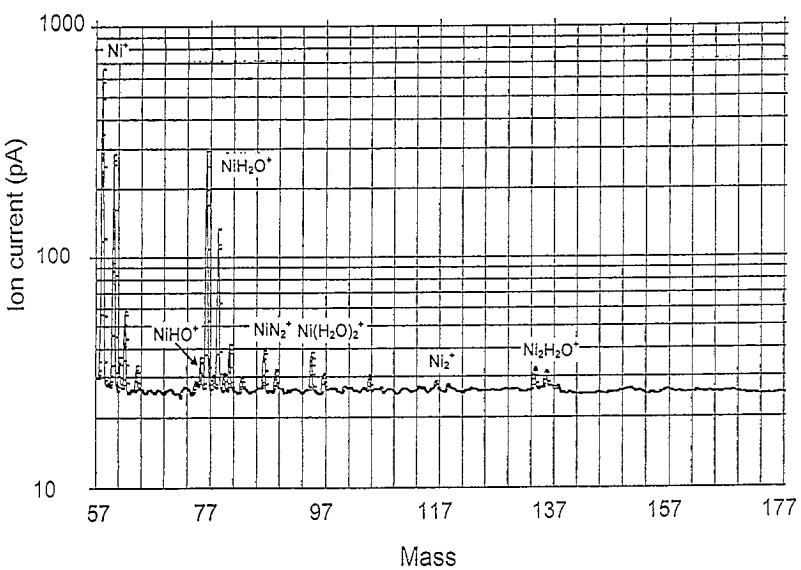

Fig. 10. A mass spectrum of ions produced inside the ion source. Lasers are tuned to the Ni resonance wavelengths (P_{He} = 100 mbar, $U_{skimmer}$ = 390 V).

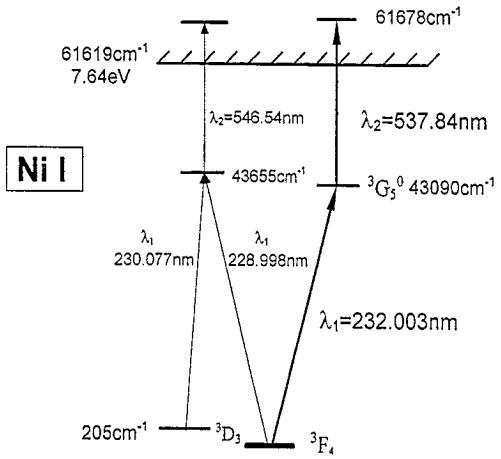

Fig. 11. A partial atomic level diagram of nickel. Wavelengths indicated on the right side were used for the on-line production of radioactive isotopes, those on the left side to probe the population of the metastable and the ground state.

equal to 1.32 MeV at a projectile beam energy of 25 MeV. This leads to an effective target thickness of 0.34 mg/cm^2 and a primary production rate of 3.6×10^4 at/μC. It has been calculated that at a He pressure of 500 mbar 100% of the nickel atoms are stopped within a distance of 2 cm. Thus no losses due to implantation in the wall of the chamber are expected.

A partial atomic level diagram of nickel is shown in Fig. 11. On the right side of the figure one can see the transitions used in the on-line experiments. Nickel atoms in the ground state $^3F_4$ are excited to the autoionizing state in two steps through the intermediate level $^3G_5^0$ ($\lambda_1 =$ 232.003 nm, $\lambda_2 = 537.84$ nm). The residence time of the radioactive nickel atoms in the ion source was studied by pulsing the cyclotron beam and monitoring the nickel atoms as a function of the delay of the laser pulse with respect to the cyclotron beam pulse. Nickel atoms were ionized by the laser beams entering the cell transversely. The cyclotron beam was pulsed 20 ms ON and 80 ms OFF and the lasers worked at 10 Hz pulse repetition rate and were triggered with a variable delay time relative to the beginning of the cyclotron beam pulse (Fig. 12a). Fig. 12b shows the count rate as a function of the laser delay time. The count rate rises up to a delay time of ~ 25 ms, since ^{55}Ni atoms need this time to reach the laser ionization zone after the beginning of the cyclotron pulse. As we can see the evacuation of radioactive atoms extends to more than 50 ms after the cyclotron beam is switched off. Next the cyclotron beam ON period was varied and the laser was fired 10 ms after switching off the cyclotron beam: the count rate builds up linearly while increasing the ON period up to ~ 30 ms but from 40 ms on, saturation is observed. This means that after 40 ms the cell is completely filled with radioactive atoms and a steady state is reached so the average residence time of radioactive atoms inside the ion source is equal to ~ 40 ms.

In the approximation of a homogeneous flow, the evacuation time of the reaction products from the ion source should be equal to $\tau_{ev} = V/C$, where $V = 9$ cm^3 is the volume of the cell between the cyclotron beam path and the exit hole and C the conductance of the exit hole. The conductance (in cm^3/s) for helium is given by the formula $C = 450\ d^2$, where d is the diameter of the hole (in mm). For $d = 0.5$ mm and $C = 112$ cm^3/s, the evacuation time τ_{ev} would be equal to 80 ms. The real flow patterns rather resemble those of a viscous flow converging towards the exit hole. Fig. 13b shows a cut of the cell with calculated lines of constant evacuation time, based on a detailed velocity distribution calculation by Berghmans and Hennissen [36]. The calculated velocity of the helium atoms on the axis of the ion source as a function of the distance from the exit hole is shown in Fig. 13a. The shaded area in Fig. 13b represents the region from which the evacuation time is longer than the diffusion time to the wall of the cell, so on average atoms originating from this region do not escape from the cell. From the figure it is clear that the signal obtained with axial laser injecting (Fig. 9a) stems mainly from atoms near the axis, and for a viscous flow the average velocity equals half of the velocity on the axis.

The count rate on mass 55 has also been measured as a function of the helium pressure (Fig. 14). The maximum count rate is observed at a helium pressure around 450 mbar. The behavior, observed in Fig. 14, is governed by three processes: (1) an increase as a function of pressure as

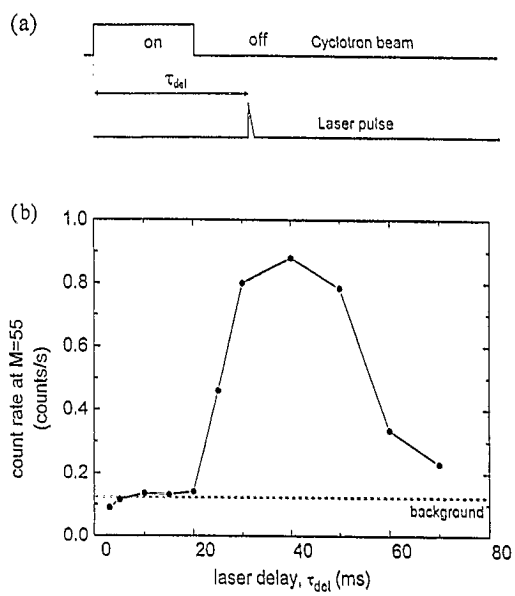

Fig. 12. The dependence of the ^{55}Ni count rate (b) as a function of the laser delay time. (a) Time structure of the measurement. Laser entrance is transverse. The He pressure is 500 mbar.

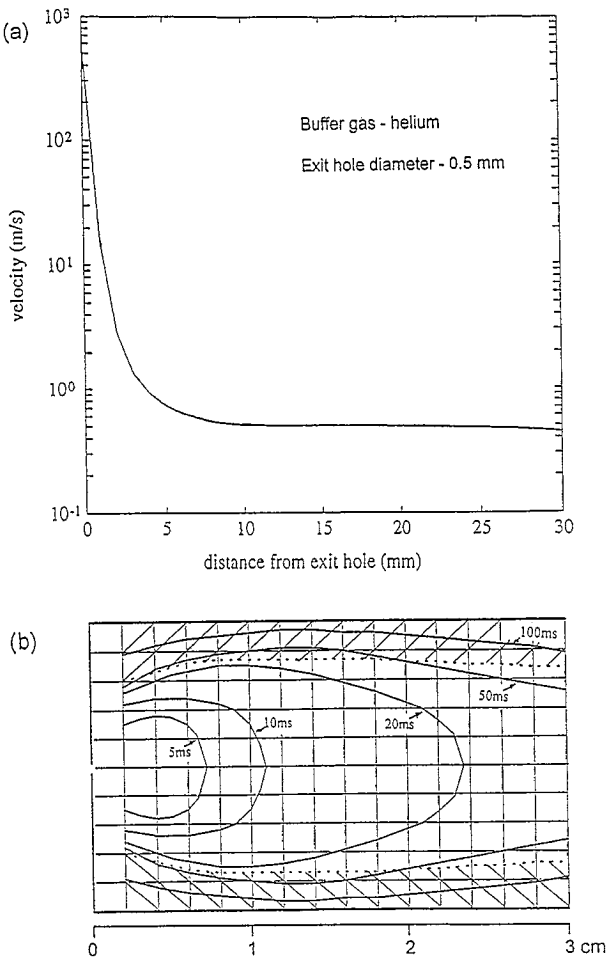

Fig. 13. (a) Calculated velocity of the helium gas flow on the axis of the ion source as a function of distance from the exit hole. (b) Two-dimensional cut of part of the gas cell with lines of equal evacuation time. Each grid line corresponds to 2 mm. The exit hole diameter is 0.5 mm. The shaded area represents the area from which the evacuation time is longer than the typical diffusion time towards the wall (at 500 mbar He).

more recoils are stopped; a saturation of this process is expected at approximately 500 mbar where all recoils are stopped inside the cell; (2) an increase as a function of pressure as the diffusion losses to the wall are decreasing; (3) a decrease as a function of pressure as the transmission through the separator deteriorates; this effect sets in around a pressure of 500 mbar.

The count rate was also checked as a function of the cyclotron beam current. A linear dependence has been observed for the cyclotron beam current from 0.1 to 1 μA.

Not all radioactive atoms are thermalized in the atomic ground state but some survive in low-lying metastable states. This fact reduces the efficiency of the source since the laser light can excite only atoms from one state at once. The relative population of the different states can be probed by subsequent tuning of the first step laser transition to a common intermediate level. The relative population of the lowest metastable state $^3D_3$, $E = 205$ cm^{-1} (Fig. 11) was measured by comparing the count rates from the ground state and this metastable state. Since the transition from the metastable state $^3D_3$ to the 43090 cm^{-1} level is forbidden by selection rules, other transitions (at 228.998 nm and 230. 077 nm) were used to excite the ^{55}Ni atoms from the ground ($^3F_4$) and metastable ($^3D_3$) states to an intermediate level of 43655 cm^{-1}. It has been verified that ionization spectra (λ_2 was scanned) are the same for both first step wavelengths and the maximum ion signal was obtained at a second step wavelength of 546.54 nm. The ratio between the count rates from the $^3D_3$ and $^3F_4$ states was as high as 0.42. This means that only 70% of the radioactive ^{55}Ni atoms were in the ground state. Similar measurement performed with stable nickel atoms produced by the filament showed the ratio between the signals from $^3D_3$ and $^3F_4$ states as high as 0.67.

A lifetime measurement was carried out on mass 55 with the lasers on resonance for nickel. The mass separator

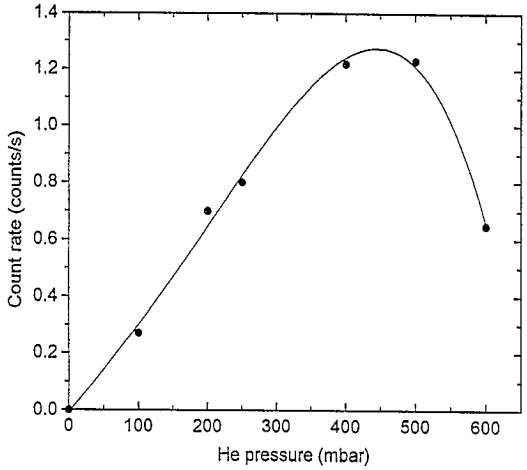

Fig. 14. Dependence of the ^{55}Ni count rate as function of the He pressure.

was additionally gated 1 s ON and 2 s OFF. For this measurement the background count rate was considerably reduced by the installation of a large plastic cosmic ray detector covering the detection system, applying coincidence conditions for $\Delta E - E$ detectors in anticoincidence with the cosmic ray detector. Fig. 15 shows the growing-in-decay curve for ^{55}Ni with the lasers on resonance (a) and off resonance (b). The fitted value for the half-life 204 ± 3 ms is in agreement with the 208 ± 5 ms published in [37] and in contradiction with our previously published value 155 ± 10 ms [15]. For more details we refer to [38].

The selectivity of the laser ion source can be defined as the ratio of the ^{55}Ni production yield with the lasers tuned on resonance to the production yield with the lasers off resonance. Comparing the total number of counts in the growing in part (Fig. 15), corrected for the background deduced from the number of counts between 2 s and 3 s, for the on-resonance and off-resonance case, a selectivity of 280^{+350}_{-100} was obtained. Such a high value for the selectivity confirms nearly full neutralization of the reaction products.

The measured mass-separated production yield was 1650 at/μC. The efficiency of the laser ion source defined as the ratio of the measured production yield to the primary ^{55}Ni production yield of 3.6×10^4 at/μC is equal to 4.6%. The contribution of the different processes to the total efficiency of the laser ion source is summarized in Table 3. Contributions 1–3 have been discussed above. In contribution 4, we assume that all radioactive atoms survive in their atomic form during the transport to the laser ionization region (efficiency $\epsilon = 100\%$). Unfortunately there is no way to check this statement. The formation of molecules due to the reaction of neutral Ni atoms with impurities cannot be tested by laser light since these

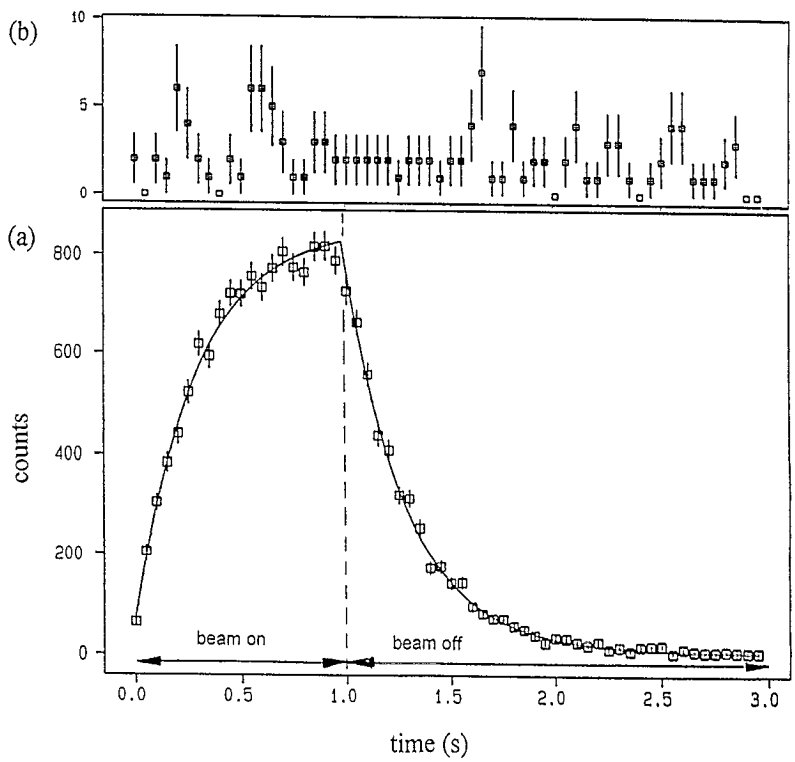

Fig. 15. Growing-in-decay curve for ^{55}Ni: (a) lasers on resonance (dose $Q = 16$ mC), (b) lasers off resonance ($Q = 6$ mC).

Table 3
Contribution of the different processes to the total efficiency of the laser ion source for ^{55}Ni ($T_{1/2}$ = 204 ms)

1.	Stopping of nuclear reaction products (500 mbar, He)	100%
2.	Neutralization	100%
3.	Thermalization in the atomic ground state	70%
4.	Survival of atoms before laser ionization against formation of molecules	100%
5.	Survival of atoms against diffusion to the cell wall	50%
6.	Laser ionization	100%
7.	Spatial overlapping of laser beams with the atomic flow at 400 Hz	60%
8.	Survival of photo ions against formation of molecular ions	74%
9.	Survival against decay losses due to transport time (40 ms)	87%
	Total estimated efficiency	13.5%
	Experimental efficiency (Experiment + cross section calculation)	4.6%

molecules are not ionized by the laser beams. From Fig. 13b it is possible to estimate the diffusion losses: for 500 mbar He it amounts up to about 50% (assuming an isotropic initial production). In point 6, we estimate the laser ionization efficiency to 100% as saturation in the first and second step is observed (Fig. 8). The efficiency of the spatial overlapping of the laser beams with the atomic flow (ϵ = 60%) has been calculated from the time profile of the stable nickel signal (Fig. 9b). In the case of transverse laser entrance the time profile should not depend on the initial distribution of the atoms inside the cell and has to be the same for stable as well as for radioactive atoms. Survival of laser produced photoions against formation of molecular ions (side bands) can be estimated from Fig. 10. The decay losses of the reaction products inside the cell is equal to 13% if we assume the average transport time 40 ms (contribution 9). Finally, we come to a total estimated efficiency of the ion source of 13.3%.

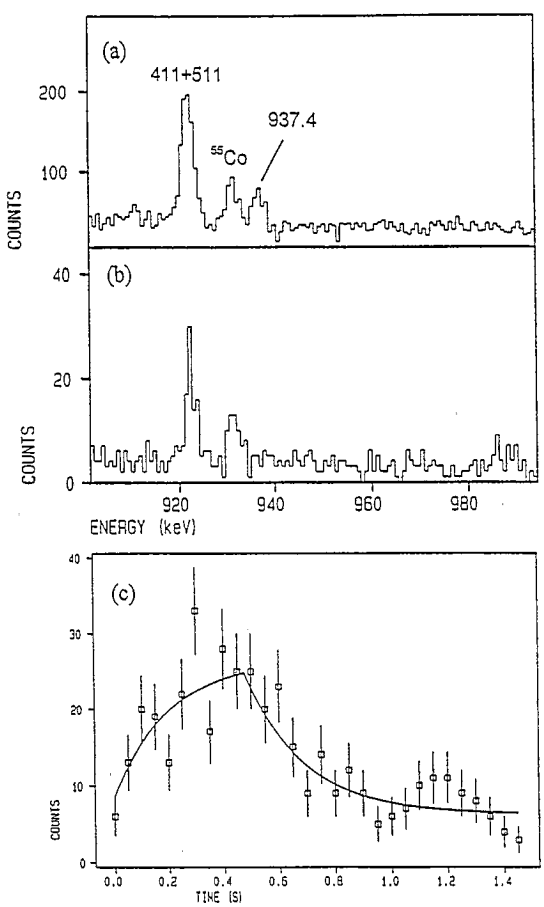

Fig. 16. β-gated γ spectrum at mass 54. The lasers are on resonance (a) and off resonance (b) with Ni; (c) the growing-in-decay curve for the 937.4 keV γ line.

5.2. The A = 54 nickel and cobalt isotopes

An analogous reaction $^{3}He^{2+}$ (45 MeV) + ^{54}Fe → ^{54}Ni, ^{54}Co has been used to produce nickel-54 and cobalt-54. The decay of ^{54}Ni has not been studied so far because its production is always overwhelmed by ^{54}Co production, of which the radioactive decay parameters are very similar to those for ^{54}Ni: the ^{54}Co ground state is a pure β emitter with a half-life of 193 ms and ^{54}Ni is expected to decay mainly via β decay to ^{54}Co and the expected half-life lies in the 100–200 ms region. The isomeric state of ^{54m}Co(7^+) has a half-life of 1.46 m and decays to an excited state in ^{54}Fe. The calculated production cross section for ^{54}Ni has a maximum of 30 μbarn at the 45 MeV helium beam energy. At this energy, the ^{54}Co production cross section is equal to 5 mbarn. Because of the high selectivity we tried to identify ^{54}Ni with the laser ion source. For the eventual assignment of γ lines to ^{54}Ni it was necessary to check the γ spectrum of ^{54m}Co. Also the ^{54}Co ground state production had to be checked to estimate its contribution to the resonant ^{54}Ni spectrum. Therefore the lasers were tuned to get resonant ionization of ^{54}Co and growing-in-decay curves as well for the ground state (separator 0.5 s ON–1 s OFF) as for ^{54m}Co (separator 180 s ON–180 s OFF) have been obtained. Again a comparison was made between the count rate on- and off-resonance; a lower limit for the selectivity of 380 was obtained. The measured mass-sep-

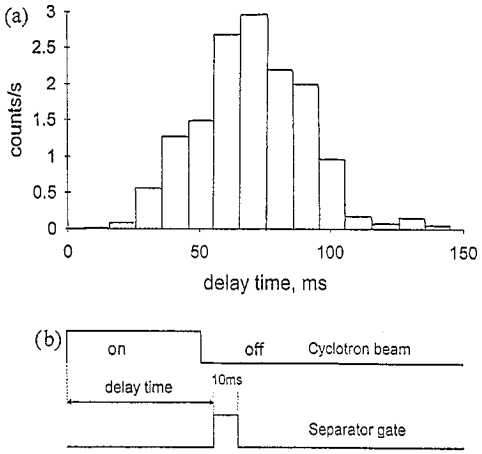

Fig. 17. Release of Rh atoms from the ion source (buffer gas is 500 mbar He). Cyclotron beam is modulated 50 ms ON, 100 ms OFF. The separator gate (10 ms) is scanned relative to the cyclotron pulse. Lasers run at 200 Hz and enter the cell in the transverse way.

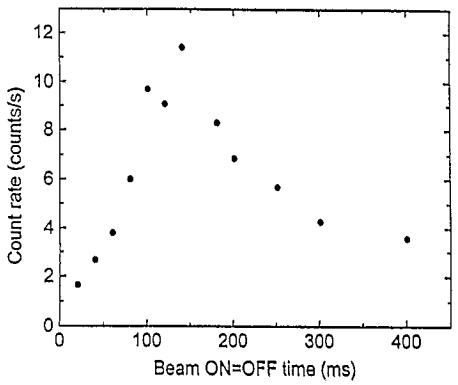

Fig. 18. The count rate versus the cyclotron beam ON period (OFF period for the same time). Buffer gas is 150 mbar Ar.

arated production yield for ^{54}Co was 7880 at/μC. The efficiency of the laser ion source based on the experimental production yield and on the calculated primary production yield (reaction cross section -5 mbarn) is equal to 6.6%.

The ^{54}Ni itself was resonantly produced and the β-gated γ spectrum at mass 54 was accumulated both with lasers ON (Fig. 16a) and OFF (Fig. 16b) resonance. A clear signature of ^{54}Ni was found: the 937.4 keV γ line is uniquely present in the laser ON spectrum. Fig. 16c shows the growing-in-decay curve from which a preliminary halflife of 143(23) ms has been deduced for ^{54}Ni.

6. Laser ionization of radioactive atoms produced in fission reactions

The performances of the ion source has also been tested for proton-induced fission reactions. The main difference with the previous case consists in the much higher recoil energy of the reaction products. The fission of uranium atoms gives two ~ 90 MeV fragments with an isotropic recoil distribution. Nuclei with this energy cannot be stopped by a permissible gas pressure (500 mbar He or 150 mbar Ar) and hence have to be slowed down in the target.

Two uranium targets were placed in a way to avoid direct view from the exit hole region in order to minimize thermalization in this region (Fig. 4). At this position of the targets, the fission fragments are stopped farther inside the cell. The A and Z-distributions of proton induced fission of ^{238}U are well known [39,40]. We concentrated our tests on ^{113}Rh which has a half-life of 2.72 s and which is produced with a cross section of 30 mbarn [39]. The rhodium atoms were ionized by the laser beams entering the cell transversely. A calculation of the rhodium energy distribution coming out of the target shows that only 1.5% of the atoms can be stopped within a distance of 2.5 cm in 500 mbar He and 2.6% in 150 mbar Ar.

The evacuation of laser-produced rhodium ions stopped in He has been studied by changing the delay between the separator gate and the cyclotron pulse (Fig. 17). The cyclotron beam was modulated 50 ms ON and 100 ms OFF. The lasers were fired at a pulse repetition rate of 200 Hz. The β count rate of ^{113}Rh isotopes was measured at different delay times of the separator gate (width 10 ms) relative to the beginning of the cyclotron beam ON period. As we can see from Fig. 17a already within the cyclotron ON-period a significant amount of ions is evacuated; the maximum is reached around 20 ms after the end of the cyclotron pulse and 50 ms after the cyclotron pulse the count rate is at the background level again. This is in contrast with argon as a buffer gas. Fig. 18 shows the

Table 4
The characteristics of the γ-rays used to deduce the Rh yields

	E_γ (keV)	ϵ_γ (%)	Absolute branching ratio (%)	I_γ	I (mass separated atoms) (relative units)
^{113}Rh	348.8	16	45	15851	2.2×10^5
^{113}Pd	643.7	9	6	1607	3.0×10^5
^{113}Ag	316.0	17	10	7582	4.5×10^5

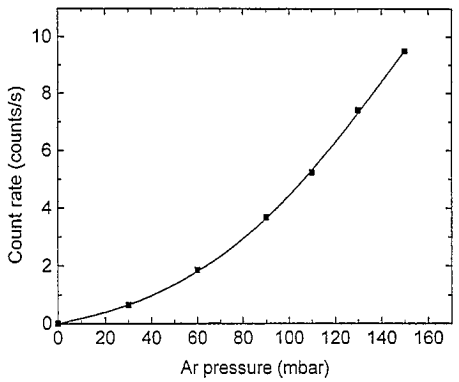

Fig. 19. The Rh count rate ($M = 113$) as a function of Ar pressure.

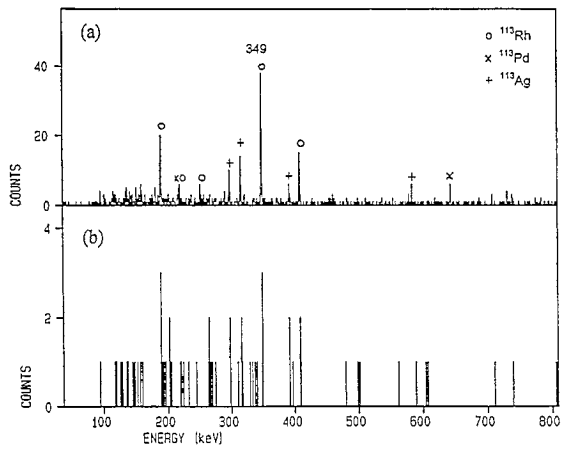

Fig. 20. β-gated γ spectrum taken at mass 113 with lasers on resonance with Rh (a) and off resonance (b). The γ lines from the directly produced ^{113}Rh and its daughter nucleus ^{113}Pd and granddaughter nucleus ^{113}Ag are clearly visible.

^{113}Rh count rate as a function of the cyclotron beam ON period at an argon pressure of 150 mbar. The beam OFF period is equal to the beam ON period and hence the same average cyclotron beam current is maintained. The maximum count rate is obtained after a much longer time than for He: about 140 ms instead of 50 ms. This is in good agreement with the ratio of the conductance of the exit hole for Ar and He.

Fig. 19 shows the count rate of the laser produced Rh ions as a function of Ar pressure. The count rate with a maximum permissible Ar pressure of 150 mbar was found to be 1.6 times higher than with 500 mbar of He. This is in good agreement with the estimated stopping efficiency of 1.5% in He and 2.6% in Ar. As can be seen even a much higher efficiency can be obtained if a higher Ar pressure could be used. For the moment this is not possible since the pressure in the skimmer region would become too high. A solution of this problem is currently worked out: a SextuPole Ion Guide [33] will be used to transport the ions from the laser ion source to the extraction electrode [34].

The maximum obtained production of ^{113}Rh was 4260 at/μC. Fig. 20 shows the β-gated γ spectra at mass 113 with the lasers ON and OFF resonance. From a comparison of the count rate in the 349 keV line of ^{113}Rh, a selectivity of 50 was obtained. Due to this selectivity, the γ spectrum (Fig. 20a) is dominated by ^{113}Rh decay: ^{113}Pd and ^{113}Ag are only present as daughter and granddaughter products. With the normal fission ion guide the spectrum at mass 113 reflects the Z distribution of the fission yield curve and the Rh, Pd and Ag are produced with roughly equal intensities [41]. The laser selectivity of 50 can be used to obtain new information on the branching ratios of γ-rays in the decay of Rh, Pd and Ag. The intensities (I_γ) of the most intense γ-rays in the decay chain Rh–Pd–Ag are given in Table 4 as obtained from a β-gated γ spectrum, taken for 1390 s. With such a counting time, no half-life corrections have to be made. By using the measured γ-ray detection efficiency (ϵ_γ) and absolute branching ratios as compiled by Jauho in his thesis work [42], relative production rates are obtained. In principle these

Table 5
Production yield, efficiency and selectivity of the laser ion source for different isotopes

Isotope ($T_{1/2}$)	Reaction (cross section)	Production at/μC out of the target [a] (calculation)	Production ions/μC in the beam [b] (experiment)	Efficiency [c] %	Selectivity [d]
^{55}Ni (204 ms)	^{54}Fe (^{3}He, $2n$)^{55}Ni (1.5 mbarn)	3.6×10^4	1650	4.6	280
^{54}Co (193 ms)	^{54}Fe (^{3}He, $2np$)^{54}Co (5 mbarn)	1.2×10^5	7880	6.6	> 380
^{113}Rh (2.7 s)	^{238}U (p,f)^{113}Rh (30 mbarn)	1.9×10^6	4260	0.22 [e]	50

[a] Number of radioactive atoms recoiling out of the target per μC of primary cyclotron beam.
[b] Number of radioactive ions in the mass separated beam per μC of primary cyclotron beam.
[c] [Ions/s in mass separated beam]/[atoms/s recoiling out the target] (%).
[d] Ions/s in mass separated beam (lasers on resonance)/ions in mass separated beam (lasers off resonance).
[e] Low value is explained by low stopping efficiency in buffer gas.

rates should be equal for all isotopes considered as only ^{113}Rh is laser ionized. It is clear that there is quite some uncertainty in the used branching ratios and the published isotope yield distribution [42] for proton-induced fission should be regarded with some care.

7. Conclusions

A new laser ion source has been successfully tested with light-ion induced fusion and proton-induced fission reactions. Table 5 summarizes the obtained results. The obtained efficiencies are typically 10 times higher than those of the standard ion guide, both for fission and fusion reactions. Additionally a selectivity around 300 for fusion and 50 for fission was reached. Although an improvement on these numbers can be expected with some modifications, already now this ion source allows to extend the study of many elements far from stability, especially in cases where isobaric contamination is the limiting factor with the previously available ion sources.

Acknowledgements

We would like to thank the cyclotron group at Louvain-la-Neuve for running and maintaining the accelerator. We also like to thank Dr. R. Kirchner for performing HIVAP calculations and Prof. Dr. Ir. J. Berghmans and Ir. J. Hennissen for performing calculations on the flow properties of helium in the ion source. This work is supported by the Belgian Inter-University Institute for Nuclear Sciences (I.I.K.W.) and by the Concerted Action (G.O.A.) and Inter-University Attraction Poles (I.U.A.P.) Research Programs. L.V. is Postdoctoral Researcher and S.F. is Research Assistant of the Belgian National Fund for Scientific Research (N.F.W.O.).

References

[1] E. Roeckl, Rep. Prog. Phys. 55 (1992) 1661.
[2] H. Ravn, Nucl. Instr. and Meth. B 70 (1992) 107.
[3] V.S. Letokhov, Laser Photoionization Spectroscopy (Academic Press, Orlando, 1987).
[4] G.S. Hurst and M.G. Payne, Principles and Applications of Resonance Ionization Spectroscopy (Hilger, London, 1988).
[5] S.V. Andreev, V.I. Mishin and S.K. Sekatskii, Sov. J. Quantum Electron. 15 (1985) 398.
[6] S.V. Andreev, V.I. Mishin and V.S. Letokhov, Opt. Commun. 57 (1986) 317.
[7] H.J. Kluge, F. Ames, W. Ruster and K. Wallmeroth, in: Proc. of the Accelerated Beams Workshop, Parksville, eds. L. Buchmann and J.M. D'Auria, TRIUMPF Report No. TRI-85-1 (1985) 119.
[8] W.M. Fairbank, Jr and H.K. Carter, Nucl. Instr. and Meth. B 26 (1987) 357.
[9] W.M. Fairbank, Jr, A. Barrera, H.K. Carter, K.R. Newton and A.C. Trivedi, Proc. of the Workshop on the Production and Use of Intense Radioactive Beams at the ISOSPIN Laboratory, 1992.
[10] G.D. Alkhazov, L.Kh. Batist, A.A. Bykov, V.D. Vitman, V.S. Letokhov, V.I. Mishin, V.N. Panteleyev, S.K. Sekatsky and V.N. Fedoseyev, Nucl. Instr. and Meth. A 306 (1991) 400.
[11] V.I. Mishin, V.N.. Fedoseyev, H.-J. Kluge, V.S. Letokhov, H.L. Ravn, F. Scheerer, Y. Shirakabe, S. Sundell and O. Tengblad, Nucl. Instr. and Meth. B 73 (1993) 550.
[12] R. Kirchner, GSI Nachrichten 05-93 (1993) 2.
[13] P. Van Duppen, P. Dendooven, M. Huyse, L. Vermeeren, Z.N. Qamhieh, R.E. Silverans and E. Vandeweert, Hyperf. Interact. 74 (1992) 193.
[14] M.Oshima, T.Sekine, S. Ichikawa, Y. Nishinaka, T. Morikawa and H. Inamura, Nucl Instr. and Meth. B 70 (1992) 241.
[15] L. Vermeeren, N. Bijnens, M. Huyse, Y.A. Kudryavtsev, P. Van Duppen, J.Wauters, Z.N. Qamhieh, P. Thoen, E. Vandeweert and R.E. Silverans, Phys. Rev. Lett. 73 (1994) 1937.
[16] J. Ärje, J. Äystö, H. Hyvonen, P. Taskinen, V. Koponen J. Honkanen, A. Hautojarvi and K. Vierinen, Phys. Rev. Lett. 54 (1985) 99.
[17] G.D. Sprouse, J. Das, T. Lauritsen, J. Schecker, A Berger, J. Billowes, C.H. Holbrow, H.-E. Mahnke and S.L. Rolston, Phys. Rev. Lett. 63 (1989) 1463.
[18] A. Berger, J. Billowes, J. Das, S. Dutta, G. Gwinner, C.H. Holbrow, T. Kuhl, T. Lauritsen, S.L. Rolston, J. Schecker, G.D. Sprouse and F. Xu, Nucl. Instr. and Meth. A 311 (1992) 24.
[19] W. Lauth, H. Backe, M. Dahlinger, I. Klaft, P. Schwamb and G. Schickert, Phys. Rev. Lett. 68 (1992) 1675
[20] H. Backe et al., Proc. of the Sixth Int. Conf. on Nuclei Far From Stability and the Ninth Conf. on Atomic Masses and Fund. Constants, eds. R. Neugart and A. Wöhr (IOP-Publishing, 1993) 151.
[21] M. Huyse, P. Decrock, P. Dendooven, J. Gentens, G. Vancraeynest, P. Van Den Bergh and P. Van Duppen, Nucl. Instr. and Meth. B 70 (1992) 50.
[22] K. Deneffe, B. Brijs, E. Coenen, J. Gentens, M. Huyse, P. Van Duppen and D. Wouters, Nucl. Instr. and Meth. B 26 (1987) 399.
[23] P. Taskinen, H. Pentilla, J. Aysto, P. Dendooven, P. Jauho, A. Jokinen and M. Yoshii, Nucl. Instr. and Meth. A 281(1989) 539.
[24] K. Niemax, Appl. Phys. B 32 (1983) 59.
[25] D. Popescu, I. Popescu and J. Richter, Z. Phys. 226 (1969) 160.
[26] T.J. Whitaker and B.A. Bushaw, Chem. Phys. Lett. 79 (1981) 506.
[27] R.H. Page and C.S. Gudeman, J. Opt. Soc. Am. B 7 (1990) 1761.
[28] W.R. Hindmarsh and J.M. Farr, Prog. Quantum Electron. 2 (1972) 186.
[29] W.H. King, Isotope Shifts in Atomic Spectra (Plenum Press, New York and London, 1984).
[30] D.L. Albritton, At. Data Nucl. Data Tabl. 22 (1978) 1.
[31] M, Rosi and C.W. Bauschlicher, Jr, J. Chem. Phys. 90 (1989) 7264; 92 (1990) 1876.
[32] W. Lindinger, T.D. Mark and F. Howorka, Swarms of Ions and Electrons in Gasses (Springer, Wien–New York, 1984).

[33] H.J. Xu, M. Wada, J. Tanaka, H. Kawakami and I. Katayama, Nucl. Instr. and Meth. A 333 (1993) 274.
[34] S. Franchoo et al., to be published.
[35] W. Reisdorf, Z. Phys. A 300 (1981) 227.
[36] J. Berghmans and J. Hennissen, private communication.
[37] J. Äystö et al., Phys. Rev. Lett. 138 B (1984) 369.
[38] I. Reusen et al., to be published.
[39] S. Baba, H. Umezawa and H. Baba, Nucl. Phys. A 175 (1971) 177.
[40] P.P. Jauho, A. Jokinen, M. Leino, J.M. Parmonen, H. Penttila, J. Äystö, K. Eskola and V.A. Rubchenya, Phys. Rev. C 49 (1994) 2036.
[41] M. Leino, P.P. Jauho, J. Äystö, P. Decrock, P. Dendooven, K. Eskola, M. Huyse, A. Jokinen, J.M. Parmonen, H. Penttila, G. Reusen, P. Taskinen, P. Van Duppen and J. Wauters, Phys. Rev. C 44 (1991) 336.
[42] P.P. Jauho, Isotope production in light charged particle induced fission, Thesis, Jyväskylä (1994).